ACADEMIC
PRESS

# Linear regression with spatial constraint to generate parametric images of ligand-receptor dynamic PET studies with a simplified reference tissue model

Yun Zhou,[a,*] Christopher J. Endres,[a] James Robert Brašić,[a] Sung-Cheng Huang,[b] and Dean F. Wong[a]

[a] *Division of Nuclear Medicine, the Russell H. Morgan Department of Radiology and Radiological Science, Johns Hopkins University School of Medicine, Baltimore, MD 21287, USA*
[b] *Department of Molecular and Medical Pharmacology, School of Medicine, University of California at Los Angeles, Los Angeles, CA, USA*

## Abstract

For the quantitative analysis of ligand-receptor dynamic positron emission tomography (PET) studies, it is often desirable to apply reference tissue methods that eliminate the need for arterial blood sampling. A common technique is to apply a simplified reference tissue model (SRTM). Applications of this method are generally based on an analytical solution of the SRTM equation with parameters estimated by nonlinear regression. In this study, we derive, based on the same assumptions used to derive the SRTM, a new set of operational equations of integral form with parameters directly estimated by conventional weighted linear regression (WLR). In addition, a linear regression with spatial constraint (LRSC) algorithm is developed for parametric imaging to reduce the effects of high noise levels in pixel time activity curves that are typical of PET dynamic data. For comparison, conventional weighted nonlinear regression with the Marquardt algorithm (WNLRM) and nonlinear ridge regression with spatial constraint (NLRRSC) were also implemented using the nonlinear analytical solution of the SRTM equation. In contrast to the other three methods, LRSC reduces the percent root mean square error of the estimated parameters, especially at higher noise levels. For estimation of binding potential (BP), WLR and LRSC show similar variance even at high noise levels, but LRSC yields a smaller bias. Results from human studies demonstrate that LRSC produces high-quality parametric images. The variance of $R_1$ and $k_2$ images generated by WLR, WNLRM, and NLRRSC can be decreased 30%–60% by using LRSC. The quality of the BP images generated by WLR and LRSC is visually comparable, and the variance of BP images generated by WNLRM can be reduced 10%–40% by WLR or LRSC. The BP estimates obtained using WLR are 3%–5% lower than those estimated by LRSC. We conclude that the new linear equations yield a reliable, computationally efficient, and robust LRSC algorithm to generate parametric images of ligand-receptor dynamic PET studies.
© 2003 Elsevier Science (USA). All rights reserved.

## Introduction

Positron emission tomography (PET) studies with neuroreceptor radioligands enable the quantification of the distribution and the binding characteristics of brain neuroreceptors. Compartmental modeling with a metabolite-corrected arterial input function is frequently utilized to rigorously quantify PET neuroreceptor studies. A typical compartmental modeling procedure is to describe tracer uptake in tissue with a three compartmental model (Fig. 1), with compartments for tracer in plasma ($C_p$), tracer that is free and nonspecifically bound in tissue ($C_{F+NS}$), and tracer that is specifically bound in tissue ($C_{SB}$). The model includes first-order rate constants that describe the transport of tracer from blood to tissue ($K_1$ (ml/min/ml)), the efflux from tissue to blood ($k_2$ (min$^{-1}$)), the rate of specific receptor binding ($k_3$ (min$^{-1}$)), and the rate of dissociation from receptors ($k_4$ (min$^{-1}$)). One common measure of neuroreceptor binding is

* Corresponding author. Division of Nuclear Medicine, Department of Radiology, Johns Hopkins University School of Medicine, 601 N. Caroline Street, JHOC room 3245, Baltimore, MD 21287-0807. Fax: +1-410-955-0696.
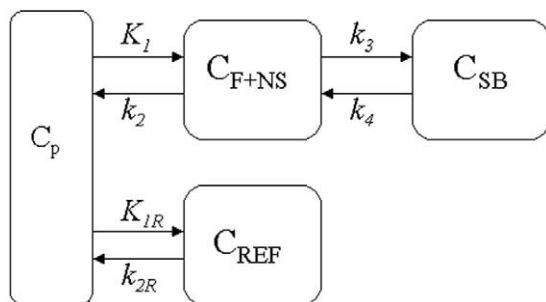*E-mail address:* yunzhou@jhmi.edu (Y. Zhou).

Fig. 1. (Top) A typical three compartmental model that is applied to ligand-receptor studies, with compartments for plasma tracer ($C_p$), tracer that is free and nonspecifically bound in tissue ($C_{F+NS}$), and tracer that is specifically bound in tissue ($C_{SB}$). (Bottom) A reference region model that uses a compartment for plasma tracer ($C_p$) and a single tissue compartment ($C_{REF}$) to represent free+nonspecific binding. For parameter definitions see text.

the total distribution volume ($DV_T$), which is defined as the ratio of the total tracer concentration in tissue ($C_T = C_{F+NS} + C_{SB}$) and plasma at equilibrium. In terms of the model parameters, $DV_T = (K_1/k_2)(1+k_3/k_4)$. It is often desirable to measure the binding potential ($BP = k_3/k_4$), which is a more direct measure of specific binding. However, estimation of BP requires measurement of the free + nonspecific distribution volume ($V_e = K_1/k_2$), which is equal to the ratio of $C_{F+NS}$ and $C_p$ at equilibrium. It is generally assumed that $V_e$ is the same in all cerebral tissue regions; therefore, $V_e$ may be estimated from a tissue region that has no specific receptor binding ($k_3 = 0$), in which case $DV_T = V_e$. Such a region that is devoid of specific receptor binding is called either a reference region or reference tissue. In principle, a reference region can be modeled with a single tissue compartment ($C_{REF}$) that represents free+nonspecific binding (Fig. 1), with blood tissue exchange parameters ($K_{1R}$, $k_{2R}$) that are related to $K_1$ and $k_2$ (in regions with specific receptor binding) by $V_e = K_{1R}/k_{2R} = K_1/k_2$.

Compartmental modeling with a plasma input function is a rigorous quantitative approach. Unfortunately it is also a laborious and complicated procedure. In addition, the required arterial sampling is a discomfort to the subject and demands additional personnel and preparation time for the PET study. Thus, there is strong motivation to develop alternatives to blood-based modeling and blood-based analytical methods in general, to allow for a simpler study protocol and to decrease the complexity of the analysis. Several quantitative methods have been developed for PET neuroreceptor studies that effectively apply a time–activity curve (TAC) derived from reference tissue in lieu of an arterial input function (Ichise et al., 1996; Lammertsma and Hume, 1996; Lammertsma et al., 1996; Logan et al., 1996; Patlak and Blasberg, 1985).

Appropriate reference tissues that are practically devoid of specific receptor binding have been identified for several neuroreceptor systems, including the cerebellum for dopamine $D_2$ ligands such as [11C]raclopride ([11C]RAC) (Farde

et al., 1989) and [11C]WIN35,428 (Wong et al., 1993), the occipital cortex for the $\mu$-opiate agonist [11C]carfentanil (Frost et al., 1989), and the pons for benzodiazepine receptor studies using [11C]flumazenil ([11C]FMZ) (Delforge et al., 1997; Koeppe et al., 1991; Millet et al., 2002). Thus reference tissue-based analytical techniques are suitable for numerous ligand-receptor PET studies (Banati et al., 1999; Blomqvist et al., 1990, 2001; Ginovart et al., 2001; Gunn et al., 1997, 1998, 2001; Lammertsma et al., 1996; Lopresti et al., 2001; Parsey et al., 2001). Perhaps the simplest reference tissue technique is the ratio method for which specific binding is estimated by dividing the tissue tracer concentrations in receptor-rich areas by the tracer concentration in a reference region (Wong et al., 1984). However, the ratio method is prone to bias (Carson et al., 1993) and is particularly not recommended when the tracer is delivered via rapid bolus injection. A more robust technique is the graphical method, which uses a transformation of the tissue data to yield a "Logan plot" that becomes linear over time (Logan et al., 1996) (Eq. (1)).

$$\frac{\int_0^t C_T(s)ds}{C_T(t)} = DV_R \frac{\int_0^t C_{REF}(s)ds + \dfrac{C_{REF}(t)}{\bar{k}_{2R}}}{C_T(t)} \tag{1}$$

$$+ \text{ int } \quad \text{for } t > t^*.$$

When used with a reference tissue input, the Logan plot has a slope that is approximately equal to the distribution volume ratio ($DV_R = DV_T/DV_{REF}$), where $\bar{k}_{2R}$ is a population average value of backflux rate constant from the reference tissue to vascular space and $DV_T$ and $DV_{REF} = V_e$ are the distribution volumes in specific binding and reference tissue regions, respectively. The BP equals $DV_R - 1$. The Logan plot offers the convenience of obtaining a measurement from a simple linear fit, although the approach to linearity depends on how rapidly the tracer achieves equilibrium. The less desirable aspects of this method include (1) the arbitrary choice of the apparently linear portion of the Logan plot for measurement and (2) the need to estimate $\bar{k}_{2R}$ using compartmental modeling with plasma input approach (Holden et al., 2001; Sossi et al., 2001). An alternative approach is to use reference tissue-based compartmental modeling, which can be derived from blood input compartmental modeling of specific binding and reference tissue regions (Lammertsma and Hume, 1996; Lammertsma et al., 1996). From the model configurations shown in Fig. 1, a reference tissue model can be derived that contains four parameters ($R_1$, $k_2$, $k_3$, $k_4$), where $R_1 = K_1/K_{1R}$ (Lammertsma et al., 1996). However, for some tracers rapid equilibrium between $C_{F+NS}$ and $C_{SB}$ allows these compartments to be described kinetically as a single compartment (Ginovart et al., 2001; Koeppe et al., 1991; Lammertsma and Hume, 1996; Lassen et al., 1996; Szabo et al, 1999). By reducing the specific binding model to a single tissue compartment (Fig. 2), a reference tissue model can be derived
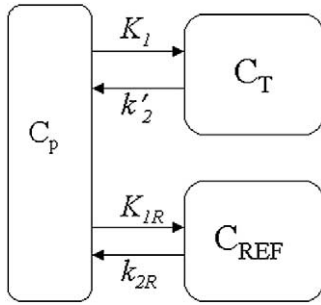
Fig. 2. The model formulations used to derive the simplified reference tissue model (SRTM). Under the assumption of rapid equilibrium between $C_{\text{F+NS}}$ and $C_{\text{SB}}$ (see Fig. 1), the total tracer concentration in specific binding regions can be modeled with a single compartment with concentration $C_{\text{T}} = C_{\text{F+NS}} + C_{\text{SB}}$. The reference tissue region is modeled with a single compartment ($C_{\text{REF}}$).

that contains only three parameters ($R_1$, $k_2$, BP) (Lammertsma et al., 1996). The three-parameter model is called the simplified reference tissue model (SRTM) and converges much more reliably than the four-parameter model. The differential equations for SRTM yield an analytical solution for the total tissue activity, $C_{\text{T}}$, given by

$$C_{\text{T}}(t) = R_1 C_{\text{REF}}(t) + (k_2 - R_1 k_2/(1 + BP))C_{\text{REF}}(t)$$

$$\otimes \exp(-k_2 t/(1 + BP)), \qquad (2)$$

where $\otimes$ represents mathematical convolution and $C_{\text{T}}(t)$ and $C_{\text{REF}}(t)$ are the tracer radioactivity concentrations measured for the target and reference tissues, respectively.

The operational equation for SRTM (Eq. (2)) includes a nonlinear macroparameter ($k_2/(1+BP)$) of SRTM and thus is usually solved by nonlinear regression when fitting TACs derived from a region of interest (ROI). Since ROI TACs are obtained by averaging over multiple pixels, the noise levels are relatively small which makes it practical to apply nonlinear fitting. However, in many cases it is desirable to perform parametric analysis on pixelwise data, which have much higher noise levels than ROI data. Although parametric imaging has been applied effectively using both linear (Blomqvist, 1984; Blomqvist et al., 1990; Carson et al., 1986; Chen et al., 1998; Feng et al., 1993; Gunn et al., 1997; Koeppe et al., 1996) and nonlinear regression (Herholz, 1987; Huang and Zhou, 1998; Kimura et al., 2002; O'Sullivan, 1994; Zhou et al., 2002c), conventional nonlinear regression is less desirable because it tends to be time consuming and provides parametric images of poor images quality, that is, either too much noise or too much resolution loss if spatial smoothing is applied. To avoid nonlinear regression for SRTM when applying Eq. (2), a basis function method has been developed by sampling discrete values of the nonlinear macroparameter ($k_2/(1+BP)$) and eliminating the two linear parameters ($R_1$ and $k_2 - R_1 k_2/(1 + BP)$) by regular linear regression (Gunn et al., 1997; Lawton and Sylvestre, 1971). The basis function method is both more computationally efficient and more robust than conventional

nonlinear regression, although the sampling procedure may introduce some bias in parameter estimates. As an alternative to using the nonlinear analytical solution of SRTM, we derive a new set of equations that are completely linear and thus can be solved using weighted linear regression directly. For comparison we have applied weighted nonlinear regression using the analytical SRTM equation. In addition, to reduce the effects of the high noise levels of the pixel TACs, parametric images generated by conventional linear or nonlinear regression can be improved by applying spatial constraints into the model fitting process (Zhou et al., 2001, 2002c). To examine this effect, we have implemented spatial constraint methods for both linear and nonlinear regression. These methods have been evaluated by computer simulation and with 16 human [11C]RAC and 9 human [11C]FMZ dynamic PET studies.

## Materials and methods

### SRTM

To obtain differential equations for SRTM, the net tracer fluxes for the specific binding ($dC_{\text{T}}/dt$) and reference tissue ($dC_{\text{REF}}/dt$) regions (Fig. 2) are expressed in terms of the model parameters and tissue concentrations (Eqs. (3) and (4)).

$$\frac{dC_{\text{T}}(t)}{dt} = K_1 C_{\text{p}}(t) - k_2' C_{\text{T}}(t) \qquad (3)$$

$$\frac{dC_{\text{REF}}(t)}{dt} = K_{1R} C_{\text{p}}(t) - k_{2R} C_{\text{REF}}(t) \qquad (4)$$

$$k_2' = k_2/(1 + BP) \qquad (5)$$

$$\frac{K_{1R}}{k_{2R}} = \frac{K_1}{k_2}. \qquad (6)$$

By solving for $C_{\text{p}}(t)$ in Eq. (4), $C_{\text{p}}(t)$ can be eliminated from Eq. (3), and then with Eqs. (5) and (6) the net rate of change of the total tissue activity $dC_{\text{T}}/dt$ can be expressed in terms of $C_{\text{REF}}(t)$, $R_1$, $k_2$, and $BP$ (Eq. (7)).

$$\frac{dC_{\text{T}}(t)}{dt} = R_1 \frac{dC_{\text{REF}}(t)}{dt} + k_2 C_{\text{REF}}(t)$$

$$- \frac{k_2}{1 + BP} C_{\text{T}}(t). \qquad (7)$$

An analytical solution of the differential equation is given by Eq. (2). Alternatively, by applying the initial condition of $C_{\text{T}}(0) = C_{\text{REF}}(0) = 0$, Eq. (7) can be integrated to give

$$C_T(t) = R_1 C_{REF}(t) + k_2 \int_0^t C_{REF}(s)ds$$

$$-k_2' \int_0^t C_T(s)ds. \tag{8}$$

The parameter that is of greatest interest is BP; however, when using Eq. (8) two regression coefficients ($k_2$, $k_2'$) must be estimated, and then BP can be calculated as $k_2/k_2' - 1$. For pixel-based computations, the high variance of estimates of $k_2'$ and $k_2$ can result in the large error propagation that is associated with division. To achieve the desired equation that enables direct estimation of BP without unstable division calculations, both sides of Eq. (8) can be multiplied through by $(1 + BP)/k_2$ and then rearranged to give

$$\int_0^t C_T(s)ds = DV_R \int_0^t C_{REF}(s)ds$$

$$+ (DV_R/(k_2/R_1))C_{REF}(t) \tag{9}$$

$$- (DV_R/k_2)C_T(t).$$

Using Eq. (9), BP can be estimated directly as $BP = DV_R - 1$.

*Linear regression with spatial constraint (LRSC)*

Eqs. (8) and (9) can be used to efficiently generate parametric images of $R_1$, $k_2$, and BP by ordinary weighted linear regression (WLR). However, we have found previously that parametric images generated by WLR may be improved by incorporating spatial information into the model fitting process (Zhou et al., 2001). The methods developed in this section are based on consideration of the propagation of measurement noise in Eqs. (8) and (9). The variables in Eqs. (8) and (9) include $C_{REF}$ and $\int_0^t C_{REF}(s)ds$, which are based on tissue ROIs, and thus should have little noise as they are obtained from averaging multiple pixels. The variable $C_T$ will have more noise than $\int_0^t C_T(s)ds$, because integration is effectively a smoothing operation. Therefore, $C_T$ is expected to be the major source of noise affecting the quality of the parametric images of $R_1$, $k_2$, and BP. Furthermore, the noise in $C_T$ is expected to propagate differently into the parameter estimates using Eqs. (8) and (9), since in Eq. (8) $C_T$ is the dependent variable, whereas in Eq. (9) it appears as an independent variable for linear regression. Consequently, we apply different noise reduction techniques to estimate the parameters of the SRTM with Eqs. (8) and (9).

*Parametric image generation algorithm using Eq. (8)*

We note that Eq. (8) is similar to the operational equation used to generate parametric images in $H_2^{15}O$ dynamic PET

studies, which are improved by a linear general ridge regression with spatial constraint technique (GRRSC) (Zhou et al., 2001). More specifically, as mentioned above $C_T$ in Eq. (8) is expected to be the largest noise contributor and is the dependent variable of linear regression, with the variables of lower noise appearing in the regression coefficient matrix $A$ ($= [C_{REF}(t) \int_0^t C_{REF}(s)ds \int_0^t C_T(s)ds]$). Thus, we chose to adapt the GRRSC technique to Eq. (8). Based on the theory of GRRSC, the columnwise parameter vector ($m{\times}1$, here $m = 3$) $\beta = [R_1, k_2, k_2']'$ is determined by minimizing the following least squares,

$$Q(\beta) = (Y - X\beta)'W(Y - X\beta)$$

$$+ (\beta - \beta_{sc})'H(\beta - \beta_{sc}), \tag{10}$$

where $'$ is the matrix transpose operation; $Y$ is a measured tissue time activity vector ($n{\times}1$); $X$ is an $n{\times}m$ matrix determined by the tracer kinetic model; $W$ is a diagonal matrix ($n{\times}n$) with positive diagonal element $w_{ii} =$ (duration of ith frame of dynamic PET scanning) for human studies; $H$ is a diagonal matrix with nonnegative diagonal elements $h_1$, $h_2$, and $h_3$ (called ridge parameters); and $\beta_{sc}$ is a pixelwise preestimated constraint. The term $(Y - X\beta)'W(Y - X\beta)$ in the cost function $Q(\beta)$ is the residual sum of squares for conventional WLR. In addition, $Q(\beta)$ includes a penalty term $(\beta - \beta_{sc})'H(\beta - \beta_{sc})$, which we compute from spatially smoothed a priori parameter estimates obtained using WLR. Thus there are two steps to obtain parametric images by GRRSC as follows.

*Step 1*

Estimate the images of $\beta_0$ and the variance $\hat\sigma^2$ by WLR, where $\beta_0 = (X'WX)^{-1}X'WY$ and $\hat\sigma^2 = (Y - X\beta_0)'W(Y - X\beta_0)/(n - m)$. $\beta_{sc}$ is then obtained by applying a spatial linear filter ($5 \times 5$, same weighting for all pixels of the filter) to $\beta_0$. The diagonal elements $h_i$ are calculated by applying the same spatial smoothing filter to the initial parameter estimates $h_{0i}$, where $h_{0i} = m\hat\sigma^2/((\beta_{0i} - \beta_{sci})'(\beta_{0i} - \beta_{sci}))$ ($i = 1, 2, 3$), and $\beta_{0i}$ and $\beta_{sci}$ are the ith elements of vector $\beta_0$ and $\beta_{sc}$, respectively. Note that the value of the ridge parameter $h_{0i}$ is automatically adjusted by the noise level of tracer kinetics and the spatial constraint is incorporated into the parametric images via ridge regression. Therefore, GRRSC is less stringent in the spatial constraint and the "smoothing" of parametric images by GRRSC is minimal and nonuniform.

*Step 2*

Generate parametric images of $\beta$ using Eq. (11).

$$\beta = (X'WX + H)^{-1}(X'WY + H\beta_{sc}). \tag{11}$$

*Parametric image generation algorithm using Eq. (9)*

In contrast to Eq. (8), the noisiest term ($C_T$) appears on the right-hand side of Eq. (9) and is therefore an independent

variable of linear regression. Thus the error in BP estimates obtained using Eq. (9) is expected to be dominated by the bias introduced from the errors in the measurement of the nxm regression matrix $A$ ( $= [\int_0^t C_{REF}(s)ds\ C_T(t)\ C_{REF}(t)]$). To reduce the bias of BP estimates obtained by linear regression, the $C_T$ on the right-hand side of Eq. (9) is substituted by its spatially smoothed value using the same spatial smoothing filter as in algorithm A. Theoretically, if the smoothed $C_T$ values are close to a constant within a ROI, then the matrix $A$ can be approximated to be the same over all pixels of the ROI, such that the mean ROI BP value obtained from parametric BP images is close to the value estimated from ROI kinetics. This can be seen from the following algebraic operation:

BP (ROI parametric) $= (\sum(A_i' W A_i)^{-1} A_i' W Y_i)/n =$ $(A'WA)^{-1}A'W(\sum Y_i/n) =$ BP (ROI kinetic) if $A_i = A$ for all pixels of the ROI.

In this study, the BP estimates obtained using Eq. (8) are compared to those estimated using Eq. (9) in the computer simulation and human studies. For reporting the BP values estimated by WLR or LRSC it is implicit that Eq. (9) is used. When Eq. (8) is used it will be stated explicitly.

*Computer simulations*

We performed computer simulations utilizing human [11C]FMZ dynamic PET studies. It was assumed that [11C]FMZ kinetics are accurately described by SRTM; therefore, Eq. (2) was used to simulate tissue [11C]FMZ kinetics. We utilized the $R_1$, $k_2$, and BP images of one slice (128 × 128) in the middle level of brain with one reference TAC adapted from one human [11C]FMZ dynamic study to simulate dynamic images using Eq. (2). The $R_1$, $k_2$, and BP images were obtained by applying a 6 × 6 × 6 full-width at half-maximum (FWHM) Gaussian filter to the parametric images generated by weighted nonlinear ridge regression with spatial constraint (NLRRSC) algorithm (Zhou et al., 2002c) in a human study. A smooth reference TAC was obtained by fitting the pons TAC to a sum of exponential functions. The scanning protocol (4 × 0.25, 4 × 0.5, 3 × 1, 2 × 2, 5 × 4, 6 × 5 total 60 min, 24 frames) is the same as used in human studies. Gaussian noise with zero mean and variance $\sigma_i^2 = \alpha C(t_i)\exp(0.693t_i/\lambda)/\Delta t_i$ was added to the pixel kinetics, where $C(t_i)$ is the mean of brain activities at frame $i$ (i.e., the same variance was added to all pixels), $\lambda$ (= 20.4 min) is the physical half-life of the tracer, $\Delta t_i$ is the length of the PET scanning interval of frame $i$, and $t_i$ is the midtime of frame $i$. Three $\alpha$ values (0.01, 0.09, and 0.36) were used to simulate three different noise levels, which we refer to as low, middle, and high noise levels. The low noise level is comparable to that of human ROI TACs, and the middle level is similar to the noise level in pixel TACs. When $\alpha = 0.09$, then mean ± SD of $100\sigma_i/C(t_i) = 76.6\ \pm$

47.0%. The simulated noise level of the reference TAC corresponded to $\alpha = 0.016$, which gave a noise level that is higher than that seen in pons for [11C]FMZ and cerebellum for [11C]RAC. When $\alpha = 0.016$, then mean ± SD of $100\sigma_i/C(t_i) = 22.1 \pm 8.7\%$. One-hundred realizations for each noise level were obtained to evaluate the statistical properties of the estimates of the parametric images. We calculated variance, bias, and root mean square error percent (RMSE%) of each pixelwise estimate. The bias and RMSE% are defined as

$$\text{Bias} = \sum_{i=1}^{N} \frac{(p_i - p)}{N}$$

$$\text{RMSE\%} = \frac{1}{p} \sqrt{\frac{\sum\limits_{i=1}^{N}(p_i - p)^2}{N - 1}},$$

where $p_i$ is the parameter estimate, $p$ is the "true" value (from noise free parametric image), and $N$ is the number of repeated realizations. Note that mean square error (MSE) consists of two components, squared bias and variance, that is, MSE = Bias$^2$ + Variance.

As a comparison, in addition to LRSC and WLR, weighted nonlinear regression using the Marquardt (WNLRM) (Marquardt, 1963) algorithm and NLRRSC (Zhou et al., 2002c) were also implemented. The initial parameter estimates were obtained by fitting SRTM to spatially smoothed (window size 10 × 10 pixel$^2$, equal weighting for all pixels) dynamic images using WNLRM with Eq. (2). The spatial parameter constraints used for NLRRSC were same as initial estimates. To derive the ridge parameters for NLRRSC, a 2-D spatial linear smoothing filter (window size 5 × 5 pixel$^2$, equal weighting for all pixels) was used. The 2-D spatial linear smoothing filter is also used for LRSC (Zhou et al., 2001). Since the noise has known variance, the weighting matrix $W$ of the diagonal element $w_{ii} = 1/\sigma_i^2$ was used for all four parametric imaging methods (LRSC, WLR, NLRRSC, and WNLRM). Eq. (2) was used for WNLRM and NLRRSC. BP images calculated as $k_2/k_2' - 1$ by WLR and LRSC using Eq. (8) were compared to those estimated directly using Eq. (9). Upper bounds were applied to WNLRM after convergence. Upper bounds were also applied to BP estimates by WLR and LRSC using Eq. (8).

Since the variance of simulated noise is spatially uniform, the RMSE% of estimates is inversely proportional to the true parameter values. To obtain the accuracy of the parameter estimates as a function of simulated noise levels, the ROI of whole gray matter region within the selected slice is applied to the images of mean, MSE, variance, Bias$^2$, and RMSE%.

*Applications to human ligand-receptor dynamic PET studies*

[11C]RAC and [11C]FMZ human dynamic PET studies were used to evaluate the performance of LRSC, WLR, WNLRM, and NLRRSC for comparison. While [11C]RAC is used to measure $D_2$-receptor density (Blomqvist et al, 1990; Endres and Carson, 1998; Farde et al., 1989; Mintun et al., 1984; Wagner et al., 1983), [11C]FMZ is used to measure central benzodiazepine receptor density (Delforge et al., 1997; Koeppe et al., 1991; Lassen et al., 1995; Price et al., 1993; Millet et al., 2002). Although [11C]RAC and [11C]FMZ exhibit a rapid uptake and a high specific/nonspecific ratio, the spatial distribution of the receptor density is markedly different (Delforge et al., 1997). We performed dynamic PET scans after intravenous bolus injection of [11C]RAC (20.4 ± 3.6 mCi (mean ± SD) of high specific activity (5.8 ± 3.7 Ci/$\mu$mol at time of injection) in 16 healthy human adult volunteers (age mean ± SD, 29 ± 8 years). We also performed dynamic PET scans after intravenous bolus injection of [11C]FMZ (activity 13.8 ± 0.6 mCi, sp. act 5.4 ± 1.4 Ci/$\mu$mol at time of injection) in 9 healthy adult volunteers (age mean ± SD, 35 ± 6 years). Dynamic PET scans were performed on a GE advance scanner with acquisition protocols of 4 × 0.25, 4 × 0.5, 3 × 1, 2 × 2, 5 × 4, and 12 × 5 min (total 90 min, 30 frames) and 4 × 0.25, 4 × 0.5, 3 × 1, 2 × 2, 5 × 4, and 6 × 5 frames (total 60 min, 24 frames) for [11C]RAC and [11C]FMZ, respectively. To facilitate the coregistration of the magnetic resonance imaging (MRI) and the PET scans and to minimize movement during the MRI and PET scans, subjects were fitted with thermoplastic face masks. The thermoplastic face mask was worn during the MRI and PET scans to maintain the head in the same position throughout each scan. Data were collected in 3-D acquisition mode. Ten-minute [68]Ge transmission scans acquired in 2-D mode were used for attenuation correction of the emission scans. Scatter correction of the 3-D emission is based on interpolation of the tails of the sinogram and then subtracting from the emission data in sinogram space (Cherry et al., 1993). Dynamic images were reconstructed using filtered back projection with a ramp filter (image size 128 × 128, pixel size 2 × 2 mm$^2$, slice thickness 4.25 mm), which resulted in a spatial resolution of about 4.5 mm FWHM at the center of the field of view. The decay-corrected reconstructed dynamic images are expressed in microcuries per milliliter. MRI scans were also obtained with a 1.5-T GE Signa system for each subject. T1-weighted magnetic resonance images were coregistered to the mean of all frames' dynamic PET images. The image registration program Register developed by the Montreal Neurologic Institute was used for MRI to PET image registration (Evans et al., 1991). The ROIs were defined on the coregistered MRI images and copied to the dynamic PET images to obtain ROI TACs for kinetic modeling. To minimize partial volume effects in the PET-MRI space, slices containing only edges of structures

were omitted, and regions were drawn within the apparent margins of structures. The caudate, putamen, and cerebellum (reference tissue) were drawn for [11C]RAC dynamic PET studies; cerebellum, frontal cortex, pons (reference tissue), and occipital cortex were drawn for [11C]FMZ dynamic PET studies.

The parametric imaging methods (LRSC, WLR, NL-RRSC, and WNLRM) were evaluated with human dynamic PET studies. The LRSC and NLRRSC used in human studies are the same as those performed for computer simulations. Since the variance of dynamic images is not known, the weighting matrix was determined by our parametric imaging experience. The diagonal element $w_{ii}$ of weighting matrix $W$ equals the duration of the $i$th frame of the dynamic PET scan (Zhou et al., 2001, 2002c). The weighting matrix $W$ for regression was used for the four parametric imaging methods and ROI kinetic modeling. Mask images were used for nonlinear parametric imaging (NLRRSC and WNLRM) to decrease computational cost. Both the standard ROI kinetic modeling and the parametric imaging using spatial normalization were used for evaluation. For comparison, ROIs were applied to both dynamic images and parametric images. The parameters estimated by fitting ROI TACs and mean ROI values on parametric images were then obtained. To evaluate the precision of Eq. (8) at low noise levels, we compare (1) parameter values estimated by fitting ROI kinetics using Eq. (2) with WNLRM and (2) parameter values estimated by fitting ROI kinetics using Eq. (8) with WLR. To compare LRSC and WLR parametric imaging results with ROI kinetic modeling, we calculate the percentage of difference between the ROI values obtained directly from the parametric images by WLR or LRSC and those estimated from ROI kinetics with WNLRM. The percentage of difference (diff%) is defined as 100 × (ROI(parametric image)-ROI(kinetic))/ROI(kinetic). For imagewise-based evaluation, all the parametric images were spatially normalized to the standard stereotaxic (Talairach) space (pixel size 2 × 2 mm$^2$, slice thickness 2 mm) using SPM99 (statistical parametric mapping software; Wellcome Department of Cognitive Neurology, London, UK). Because more structural information is contained in the $R_1$ images, the $R_1$ images generated by LRSC were used to determine the parameters of spatial normalization and applied to all generated parametric images for each subject. Two iterations of the spatial normalization process were performed: (1) the parameters obtained by normalizing $R_1$ images to the cerebral blood flow template provided by SPM99 and (2) the means of $R_1$ images obtained by the first iteration were used as a template for the second iteration. The sinc interpolation method was used to minimize the smoothing effect of spatial normalization. The mean and variance of $R_1$, $k_2$, and BP parametric images for all four methods were calculated in stereotaxic space. The variance analysis in human studies is based on two assumptions: (1) the variance of estimates in standard space consists of two linear components, the variance of estimates in the original PET image space and the

variance due to the spatial normalization process, and (2) the variance from the spatial normalization process is the same over different parametric imaging methods. Let $V_i$ be the pixel value of variance images generated in the standard space, $V_{0i}$ be the variance of estimates in the original PET image space, and $V_{sn}$ be the variance from the spatial normalization process. Then based on the above assumptions, we have $V_i = V_{0i} + V_{sn}$, and the difference in variance between parametric imaging methods $i$ and $j$ in the standard space $V_i - V_j$ equals the variance difference $V_{0i} - V_{0j}$ in the original PET image space. Consequently, we use $100(V_i - V_j)/V_i$ to approximate $100(V_{0i} - V_{0j})/V_{0i}$ to describe the difference in variance of estimates obtained with the different methods. A few ROIs or brain tissues used to represent low- and high-receptor-density regions are defined on the PET template in the standard stereotaxic (Talairach) space. ROIs of the caudate putamen are utilized for [$^{11}$C]RAC, and ROIs of cerebellum, frontal cortex, occipital cortex, and thalamus are utilized for [$^{11}$C]FMZ. ROI values are obtained by copying ROI to parametric mean and variance images.

All parametric imaging methods were written in MAT-LAB (The MathWorks Inc.) code and implemented on an Ultra 60 SPARC workstation.

## Results

### Computer simulations

Comparison of accuracy and precision of estimates is illustrated in Table 1. Table 1 is the gray matter-averaged mean, squared bias, variance, and RMSE% of parameter estimates at different noise levels. The squared bias, variance, mean square error, and RMSE% increase as noise level increases for all estimates, and LRSC estimates (for BP, Eq. (9) used) is of lowest increasing rate. Comparing the BP estimates obtained by LRSC using Eq. (8) to those using Eq. (9), the BP estimates obtained using Eq. (8) show more variance and higher RMSE%, although the bias was reduced at middle ($\alpha = 0.09$) and high noise ($\alpha = 0.16$) levels. A similar increase in BP variance and RMSE% with Eq. (8) was found with WLR, except when fitting a low-noise ($\alpha = 0.01$) TAC for which WLR using Eq. (8) gave almost same RMSE% with WLR using Eq. (9). The BP estimates obtained with WLR and LRSC showed similar variance, which was lower than the variance measured with the nonlinear methods (NLRRSC, WLNRM) at middle and high noise levels. Both NLRRSC and WLNRM performed well with low TAC noise; however, the large variances measured at middle and high noise levels indicates that these methods are not as suitable for modeling pixel data. As expected, NLRRSC and WLNRM do show lower bias than WLR. In fact the squared bias of NLRRSC and WL-NRM BP estimates is less than 10% of MSE for all simulated noise levels. By contrast, the squared bias of WLR BP

estimates is about 60%–82% of MSE at different noise levels. Thus the error in BP estimates obtained by WLR (using Eq. (9)) is mostly due to bias. The squared bias of BP estimated with WLR can be decreased by 60%–95% if LRSC is used without increased variance. The BP is underestimated by both WLR and LRSC, and the underestimation tends to be larger as the noise level of the TAC increases. At the middle noise level, the Bias% of the BP WLR estimates in gray matter ranges from −5% to −25% with mean of −11.9%, and the mean of underestimation is reduced to −4.4% by LRSC with ranges ~0% to 10%. On average, the BP estimated by WLR is ~3%–8% lower than those estimated by LRSC for gray matter for different noise level. The LRSC method also gave the lowest RMSE% for $R_1$ and $k_2$. In comparing LRSC and WLR, the larger RMSE% for $R_1$ and $k_2$ found with WLR is mostly due to a larger variance. This is in contrast with the results for estimating BP for which LRSC and WLR showed similar variance, but WLR had a larger bias. The average RMSE% of LRSC estimates of $R_1$ and $k_2$ is about 40%–60% less than those of WLR, NLRRSC, and WNLRM at the middle noise level.

Table 1 also shows that all methods give a similar relative increase in RMSE% because of noise in the reference TAC. Noise in the reference TAC increases both the bias and the variance of estimates, although a greater effect is seen in the bias, especially for pixel TACs with low noise levels. For pixel TACs with low noise levels, RMSE% of BP estimates obtained with middle noise level of reference TAC is about double those estimated with noise free reference TAC. The variance of estimates of $k_2$ is more sensitive to the middle or high noise in the tissue TAC. As the noise level of pixel TAC increases, the variance of estimates of $R_1$ or BP contributed by the errors in the reference TAC tends to decrease, while the variance of the estimates of $k_2$ contributed by the errors in the reference TAC keeps increasing. We also performed simulation study with the reference TAC of low noise level, which is comparable to the noise level of ROI TACs. The results from reference TAC of low noise level ($\alpha = 0.01$) are almost same as those obtained with reference TAC of noise free.

### Human studies

Fig. 3 illustrates that the nonlinear estimators of $R_1$, $k_2$, and BP using Eq. (2) are almost identical to those estimated by fitting ROI kinetics using Eq. (8) with conventional WLR. This result is consistent with that obtained in the computer simulation and demonstrates that the bias introduced from the linear operational equation is negligible when applied to data of low noise level.

For comparison the results of LRSC and WLR and ROI kinetic analysis are illustrated in Figs. 4 and 5. Fig. 4 shows that for both [$^{11}$C]RAC and [$^{11}$C]FMZ dynamic PET studies, the ROI values calculated directly from parametric images generated by LRSC have high linear correlations with those estimated from ROI kinetics by WNLRM using

Table 1
Gray matter averaged mean, mean square error, squared bias, variance, and RMSE% of estimates from [$^{11}$C]FMZ simulation studies with 100 realizations for each noise level

| Estimates | Noise level $\alpha$ | Reference TAC of noise free | | | | | Reference TAC of noise level of $\alpha=0.016$ | | | | |
|---|---|---|---|---|---|---|---|---|---|---|---|
| | | Mean | MSE | Bias$^2$ (% of MSE) | Variance (% of MSE) | RMSE% | Mean | MSE | Bias$^2$ (% of MSE) | Variance (% of MSE) | RMSE% |
| *BP* by LRSC | 0.01 | 2.81 | 0.0046 | 0.0007 (15.4) | 0.0039 (84.6) | 2.9 | 2.64 | 0.0613 | 0.0392 (64.3) | 0.0217 (35.7) | 8.7 |
| | 0.09 | 2.70 | 0.0523 | 0.0219 (42.1) | 0.0301 (57.9) | 9.2 | 2.59 | 0.1122 | 0.0658 (58.9) | 0.0458 (41.1) | 12.5 |
| | 0.36 | 2.56 | 0.1915 | 0.0955 (50.1) | 0.0950 (49.9) | 17.2 | 2.52 | 0.2384 | 0.1247 (52.6) | 0.1124 (47.4) | 18.8 |
| *BP* by LRSC (Eq. (8)) | 0.01 | 2.86 | 0.0077 | 0.0019 (24.1) | 0.0059 (75.9) | 3.7 | 2.81 | 0.0346 | 0.0014 (4.1) | 0.0332 (95.9) | 7.2 |
| | 0.09 | 2.93 | 0.0742 | 0.0145 (19.5) | 0.0596 (80.5) | 12.8 | 2.88 | 0.1513 | 0.0076 (5.0) | 0.1437 (95.0) | 18.8 |
| | 0.36 | 3.27 | 1.2141 | 0.2834 (23.4) | 0.9278 (76.6) | 56.1 | 3.17 | 1.6072 | 0.1964 (12.2) | 1.4088 (87.8) | 63.0 |
| *BP* by WLR | 0.01 | 2.73 | 0.0186 | 0.0111 (60.1) | 0.0074 (39.9) | 5.1 | 2.60 | 0.0823 | 0.0578 (70.7) | 0.0239 (29.3) | 10.2 |
| | 0.09 | 2.48 | 0.1768 | 0.1443 (82.3) | 0.0310 (17.7) | 14.9 | 2.45 | 0.2215 | 0.1697 (77.2) | 0.0501 (22.8) | 16.7 |
| | 0.36 | 2.40 | 0.3349 | 0.2444 (73.5) | 0.0881 (26.5) | 21.0 | 2.39 | 0.3689 | 0.2542 (69.4) | 0.1122 (30.6) | 22.1 |
| *BP* by WLR (Eq. (8)) | 0.01 | 2.85 | 0.0089 | 0.0008 (8.7) | 0.0081 (91.3) | 4.0 | 2.79 | 0.0410 | 0.0016 (4.0) | 0.0394 (96.0) | 8.4 |
| | 0.09 | 2.94 | 0.3133 | 0.0251 (8.0) | 0.2880 (92.0) | 28.1 | 2.87 | 0.4339 | 0.0185 (4.3) | 0.4152 (95.7) | 32.0 |
| | 0.36 | 3.17 | 3.3945 | 0.3406 (10.0) | 3.0504 (90.0) | 88.1 | 3.05 | 3.3643 | 0.2865 (8.5) | 3.0750 (91.5) | 87.6 |
| *BP* by NLRRSC | 0.01 | 2.83 | 0.0076 | 0.0033 (43.0) | 0.0043 (57.0) | 3.8 | 2.73 | 0.0421 | 0.0130 (31.0) | 0.0289 (69.0) | 7.7 |
| | 0.09 | 2.85 | 0.0445 | 0.0044 (9.9) | 0.0401 (90.1) | 9.2 | 2.73 | 0.0747 | 0.0136 (18.3) | 0.0609 (81.7) | 11.0 |
| | 0.36 | 2.90 | 0.2014 | 0.0172 (8.5) | 0.1840 (91.5) | 19.7 | 2.78 | 0.1991 | 0.0146 (7.3) | 0.1843 (92.7) | 19.0 |
| *BP* by WNLRM | 0.01 | 2.82 | 0.0088 | 0.0001 (1.2) | 0.0087 (98.8) | 3.9 | 2.70 | 0.0494 | 0.0152 (30.8) | 0.0341 (69.2) | 9.0 |
| | 0.09 | 2.87 | 0.1400 | 0.0050 (3.6) | 0.1350 (96.4) | 16.6 | 2.74 | 0.1468 | 0.0099 (6.7) | 0.1368 (93.3) | 16.5 |
| | 0.36 | 3.14 | 1.2750 | 0.1318 (10.3) | 1.1419 (89.7) | 50.2 | 2.94 | 0.9595 | 0.0362 (3.8) | 0.9229 (96.2) | 42.8 |
| $R_1$ by LRSC | 0.01 | 1.29 | 0.0026 | 0.0016 (62.2) | 0.0010 (37.8) | 3.9 | 1.14 | 0.0575 | 0.0265 (46.3) | 0.0307 (53.7) | 17.9 |
| | 0.09 | 1.36 | 0.0160 | 0.0094 (59.0) | 0.0065 (41.0) | 9.9 | 1.22 | 0.0479 | 0.0109 (22.7) | 0.0369 (77.3) | 16.7 |
| | 0.36 | 1.53 | 0.0825 | 0.0648 (79.2) | 0.0171 (20.8) | 23.5 | 1.38 | 0.0621 | 0.0147 (23.7) | 0.0473 (76.3) | 20.2 |
| $R_1$ by WLR | 0.01 | 1.31 | 0.0108 | 0.0009 (8.8) | 0.0099 (91.2) | 8.4 | 1.16 | 0.0596 | 0.0186 (31.4) | 0.0407 (68.6) | 18.7 |
| | 0.09 | 1.38 | 0.0897 | 0.0120 (13.4) | 0.0775 (86.6) | 24.0 | 1.23 | 0.1116 | 0.0070 (6.3) | 0.1045 (93.7) | 26.4 |
| | 0.36 | 1.55 | 0.2915 | 0.0752 (25.8) | 0.2156 (74.2) | 43.6 | 1.40 | 0.2519 | 0.0177 (7.0) | 0.2340 (93.0) | 40.2 |
| $R_1$ by NLRRSC | 0.01 | 1.35 | 0.0152 | 0.0067 (44.3) | 0.0085 (55.7) | 9.7 | 1.14 | 0.0658 | 0.0238 (36.2) | 0.0418 (63.8) | 20.0 |
| | 0.09 | 1.37 | 0.0798 | 0.0083 (10.4) | 0.0714 (89.6) | 22.7 | 1.16 | 0.1215 | 0.0187 (15.4) | 0.1026 (84.6) | 27.6 |
| | 0.36 | 1.47 | 0.2527 | 0.0356 (14.1) | 0.2167 (85.9) | 40.4 | 1.27 | 0.2530 | 0.0063 (2.5) | 0.2466 (97.5) | 40.0 |
| $R_1$ by WNLRM | 0.01 | 1.29 | 0.0118 | 0.0001 (1.1) | 0.0117 (98.9) | 8.8 | 1.06 | 0.1053 | 0.0567 (54.2) | 0.0480 (45.8) | 24.4 |
| | 0.09 | 1.28 | 0.1015 | 0.0014 (1.4) | 0.1001 (98.6) | 25.6 | 1.07 | 0.1883 | 0.0553 (29.5) | 0.1324 (70.5) | 33.7 |
| | 0.36 | 1.37 | 0.3133 | 0.0116 (3.7) | 0.3016 (96.3) | 44.9 | 1.15 | 0.3537 | 0.0311 (8.8) | 0.3222 (91.2) | 46.8 |
| $k_2$ by LRSC | 0.01 | 0.26 | 0.0002 | 0.0001 (59.9) | 0.0001 (40.1) | 4.2 | 0.29 | 0.0037 | 0.0009 (25.7) | 0.0027 (74.3) | 19.5 |
| | 0.09 | 0.25 | 0.0026 | 0.0021 (81.6) | 0.0005 (18.4) | 11.8 | 0.27 | 0.0043 | 0.0019 (43.0) | 0.0025 (57.0) | 20.2 |
| | 0.36 | 0.20 | 0.0116 | 0.0104 (90.2) | 0.0011 (9.8) | 27.8 | 0.22 | 0.0129 | 0.0099 (77.4) | 0.0029 (22.6) | 30.0 |
| $k_2$ by WLR | 0.01 | 0.27 | 0.0008 | 0.0001 (8.5) | 0.0008 (91.5) | 8.9 | 0.30 | 0.0054 | 0.0013 (23.3) | 0.0042 (76.7) | 22.7 |
| | 0.09 | 0.25 | 0.0067 | 0.0020 (29.2) | 0.0047 (70.8) | 25.9 | 0.28 | 0.0111 | 0.0021 (18.7) | 0.0090 (81.3) | 33.7 |
| | 0.36 | 0.21 | 0.0227 | 0.0101 (44.5) | 0.0125 (55.5) | 50.0 | 0.23 | 0.0288 | 0.0100 (34.8) | 0.0187 (65.2) | 56.3 |
| $k_2$ by NLRRSC | 0.01 | 0.26 | 0.0011 | 0.0005 (49.1) | 0.0005 (50.9) | 9.7 | 0.32 | 0.0105 | 0.0035 (33.6) | 0.0070 (66.4) | 33.2 |
| | 0.09 | 0.26 | 0.0053 | 0.0004 (8.5) | 0.0048 (91.5) | 25.6 | 0.31 | 0.0148 | 0.0031 (20.8) | 0.0117 (79.2) | 43.0 |
| | 0.36 | 0.26 | 0.0138 | 0.0007 (5.4) | 0.0130 (94.6) | 43.1 | 0.31 | 0.0256 | 0.0028 (10.9) | 0.0228 (89.1) | 60.7 |
| $k_2$ by WNLRM | 0.01 | 0.27 | 0.0016 | 0.0000 (2.9) | 0.0015 (97.1) | 11.0 | 0.33 | 0.0170 | 0.0069 (40.6) | 0.0100 (59.4) | 38.2 |
| | 0.09 | 0.28 | 0.0118 | 0.0005 (3.8) | 0.0113 (96.2) | 34.7 | 0.33 | 0.0247 | 0.0059 (24.1) | 0.0187 (75.9) | 54.9 |
| | 0.36 | 0.28 | 0.0297 | 0.0007 (2.3) | 0.0290 (97.7) | 65.3 | 0.33 | 0.0445 | 0.0053 (12.0) | 0.0391 (88.0) | 82.0 |

Eq. (2), especially for BP with $R^2 > 0.99$. In addition, all the slopes of regression in Fig. 4 are not significantly different from 1 (*T* test, $P > 0.7$ for [$^{11}$C]FMZ; $P = 0.13$, 0.16, and 0.67 for $R_1$, $k_2$, and BP, respectively, for [$^{11}$C]RAC). Fig. 5 shows that the percent differences between the ROI estimators of parametric imaging and conventional ROI kinetic modeling are less than 10%. The LRSC parametric imaging method provides a smaller difference (<5%) when compared to the WLR parametric imaging method for $R_1$, $k_2$, and BP. As predicted from the theory, there is no significant difference (paired *T* test, $P > 0.90$ for all ROIs) between the ROI BP values obtained from ROI kinetic analysis and

those obtained from the parametric images generated by LRSC. However, the ROI BP values generated by WLR are significantly (paired *T* test, $P < 0.0001$) lower than those estimated by ROI kinetic modeling. Figs. 3 and 4 show that at low noise levels, the BP values estimated using either Eq. (8) or Eq. (9) are same as those estimated by ROI kinetic modeling with Eq. (2). However, differences between Eq. (8) and Eq. (9) for estimating BP are easily seen when they are applied to high noise level pixel TACs. As a specific example, Fig. 6 shows that the BP images generated by linear regression using Eq. (9), and NLRRSC are visually comparable with a similar noise level. By contrast, the BP
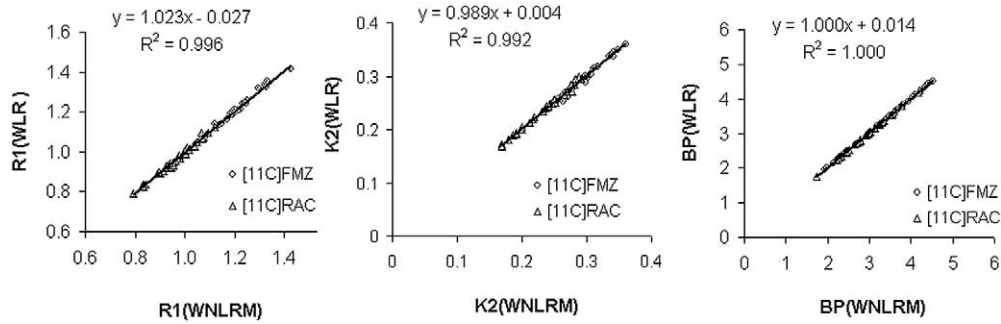
Fig. 3. $R_1$, $k_2$, and BP estimated by weighted nonlinear regression with the Marquardt (WNLRM) algorithm with Eq. (2) versus those estimated by weighted linear regression (WLR) using Eq. (8) for the kinetic analysis of regions of interest (ROIs, see materials and methods for ROIs determination).

images generated with either linear regression using Eq. (8) or WNLRM show outliers (bounds applied for image display purpose) that are due to error propagation. The distribution of these outliers is mostly on the white matter or outside of brain, the regions of lower signal-to-noise ratio, but is not limited in these regions. The pixel values of the BP image estimated by WLR using Eq. (9) are approximately 3%–5% lower than those generated by LRSC using Eq. (9) (Fig. 5). These results are further verified by the statistical analysis of parametric images in the following section.

The pixelwise evaluation of parametric imaging methods is shown in Fig. 7, which shows one plane of mean (Fig. 7A) and variance (Fig. 7B) images of $R_1$, $k_2$, and BP generated from nine human [11C]FMZ dynamic PET studies.

The BP images generated with LRSC, WLR, and NLRSSC show similar image quality and magnitude of variance. For $R_1$ and $k_2$, LRSC provides parametric images of lowest variance, with comparable or better visual quality of mean images. For all parameters, images generated using WN-LRM showed the largest variance. Similar results were obtained for the mean and variance of parametric images generated from [11C]RAC human dynamic studies. The volumes of ROIs shown in Table 2 are comparable to the ROI volumes obtained in the original PET-MRI space. The ROI values from the parametric mean and variance images are listed in Table 2. For [11C]FMZ the frontal and occipital cortices have high BP, while the caudate and putamen have low BP. Usually, BP is directly proportional to the receptor density, and the noise level of TAC in low-receptor-density
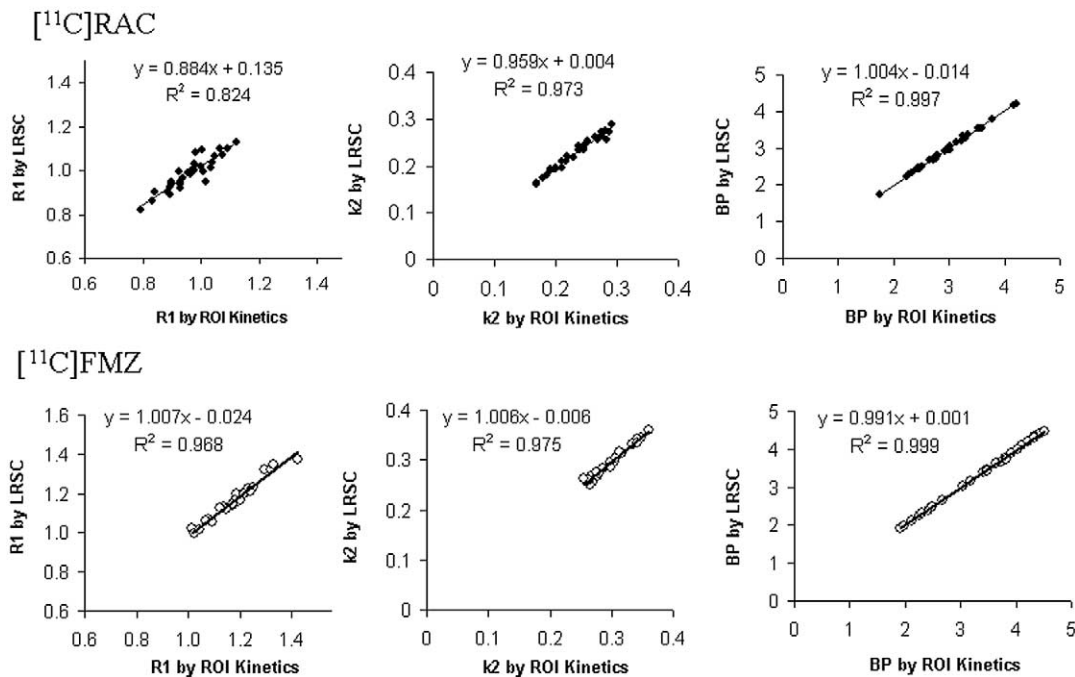


Fig. 4. Linear correlation between the region of interest (ROI, see Materials and methods for ROI determination) values calculated directly from parametric images generated by linear regression with spatial constraint (LRSC) and the values estimated from ROI kinetics by a weighted nonlinear regression with the Marquardt (WNLRM) algorithm.
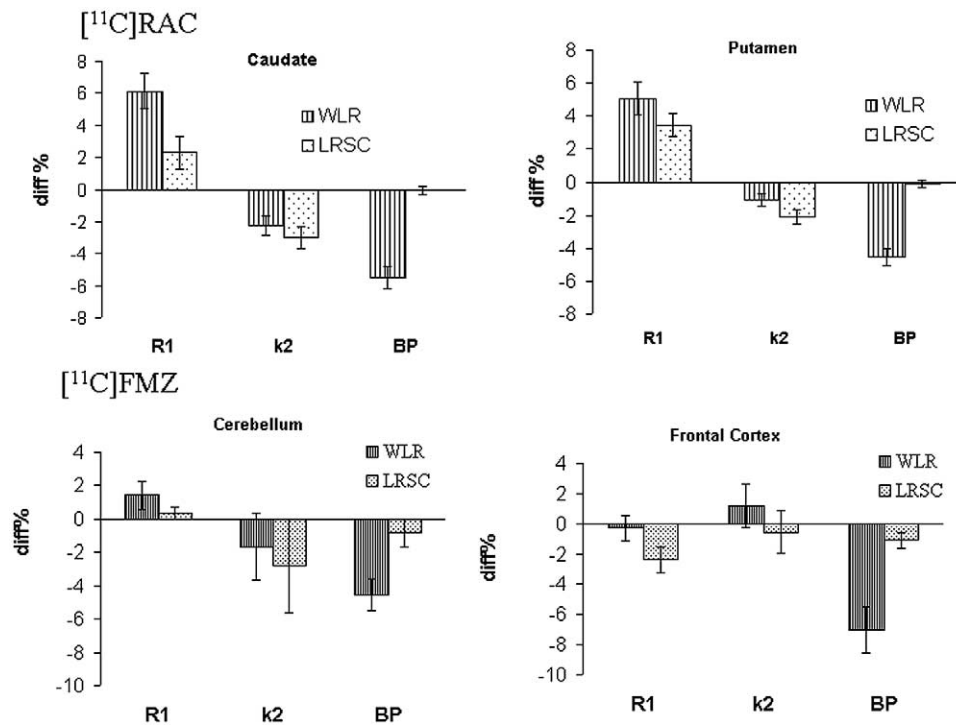
Fig. 5. The mean ± standard error of mean ($n = 9$ and $n = 16$ for [11C]RAC and [11C]FMZ respectively) of percent difference (diff%) between (1) the region of interest (ROI, see Materials and methods for ROI determination) values calculated directly from the parametric images by weighted linear regression (WLR) and linear regression with spatial constraint (LRSC) and (2) those estimated from ROI kinetics by a weighted nonlinear regression with the Marquardt (WNLRM) algorithm.

regions is higher than those at high receptor density regions (Endres and Carson, 1998; Koeppe et al., 1991; Slifstein and Laruelle, 2000). With [11C]FMZ BP estimates obtained using WNLRM taken as "true" values, the estimated Bias% of BP obtained with WLR, LRSC, and NLRRSC is found to be higher in caudate and putamen than in frontal and occipital cortices. Overall, the parametric images generated by LRSC are of lowest variance. The BP images generated by WLR and LRSC show similar variance which is ~10%–40% lower than that generated by WNLRM. Table 2 also

shows that the variance of BP images generated by WLR or LRSC with Eq. (8) is more than 20% larger compared to the variance obtained with Eq. (9). The reduced variance that is obtained with Eq. (9), in addition to the decreased occurrence of outliers (Fig. 6), supports our initial assertion that Eq. (9) is preferable to Eq. (8) for estimation of BP. The BP estimates obtained using WLR are ~3%–5% lower than those estimated by LRSC. For $R_1$ and $k_2$, the variance of WLR, NLRRSC, and WNLRM can be decreased about 30%–60% by using LRSC. These results are quite consis-
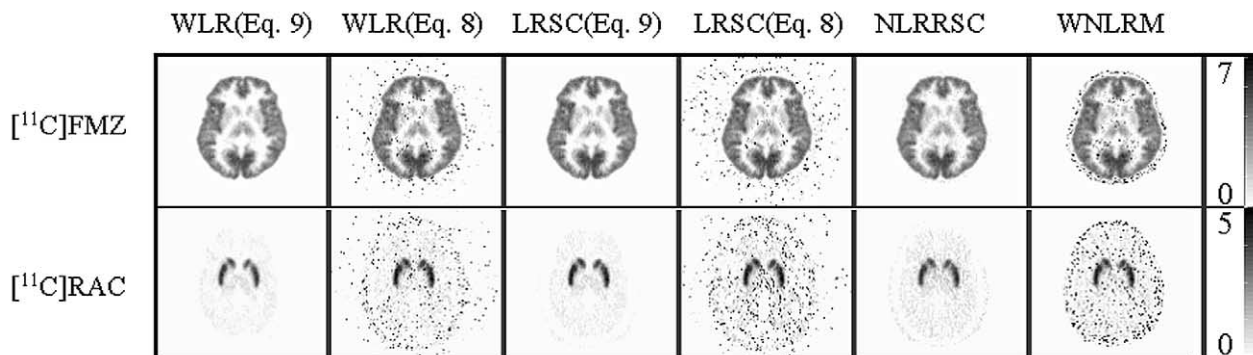


Fig. 6. (Left to right) Binding potential images generated by weighted linear regression (WLR), WLR using Eq. (8), linear regression with spatial constraint (LRSC), LRSC using Eq. (8), nonlinear ridge regression with spatial constraint (NLRRSC), and weighted nonlinear regression with the Marquardt (WNLRM) algorithm in one human [11C]flumazenil (top row) and one human [11C]raclopride (bottom row) dynamic PET studies.
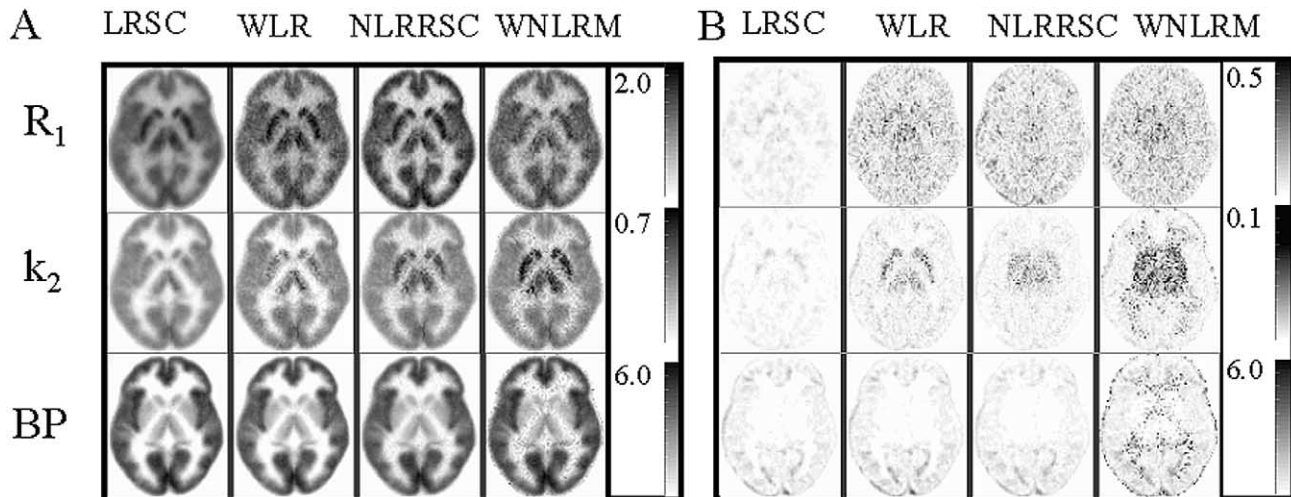
Fig. 7. Pixelwise mean (A) and variance (B) of estimates of $R_1$ (top row), $k_2$ (middle row), and binding potential (BP) (bottom) generated from the nine human [$^{11}$C]flumazenil ([$^{11}$C]FMZ) dynamic PET studies. (Left to right) Linear regression with spatial constraint (LRSC), weighted linear regression (WLR), nonlinear ridge regression with spatial constraint (NLRRSC), and weighted nonlinear regression with the Marquardt (WNLRM) algorithm.

tent with the results from the comparison between linear parametric imaging methods and ROI kinetic analysis (see Fig. 5), as well as our computer simulations (Table 1).

For each human study, it takes about 20–30 s to generate parametric images by LRSC or WLR for each plane. NLRRSC and WNLRM take about three to six times longer to run than LRSC or WLR on Ultra 60 SPARC workstation.

## Discussion

The derivation of the SRTM includes the assumption that the free+nonspecific and specific binding compartments are in rapid equilibrium. It is further assumed that there is negligible specific binding in the reference region. All methods based on SRTM, including nonlinear methods and the linear methods presented here, will be similarly affected by the limitations of these assumptions. In addition, the blood volume term is ignored in the SRTM, producing a systematic underestimation of BP regardless of which SRTM method is implemented. For example, the BP estimates obtained by SRTM underestimate the BP estimates obtained using a standard two-tissue compartmental model (Fig. 1). The underestimation may result from model simplification and assumption of the negligible radioactivity of vascular space in both reference tissue and target tissue. For [$^{11}$C]FMZ studies, the pons may not be completely devoid of specific receptor binding (Delforge et al., 1997; Price et al., 1993). The correction of the bias due to specific binding in the reference tissue is usually based on a more complex experimental protocol with additional scans to estimate BP or nonspecific distribution volume of the reference tissue (Delforge et al., 1997; Lopresti et al., 2001). However, the theoretical linear relationship verified by our studies (Fig. 8) and other previous studies (Gunn et al., 1997, 2001; Lam-

mertsma and Hume, 1996; Millet al., 2002) demonstrate that SRTM is a reliable quantification method for studying the changes in BP induced by psychological stimulation or pharmacological challenges.

The results from computer simulation of [$^{11}$C]FMZ in the present study are generally consistent with those obtained from human [$^{11}$C]FMZ PET data. In the computer simulation, we found that high noise in the reference TAC can add both bias and variance to the parameter estimates, especially for a tissue TAC of low noise level. In this study, we also simulated the reference TAC of low noise level ($\alpha = 0.01$) and found that the effects on estimates is almost negligible. This suggests that some preprocessing, such as smoothing the reference tissue TAC, may be helpful in some special situations. For example, if the reference TAC derived from a small region such as pons is quite noisy due to movement during PET scan, then movement correction or temporal smoothing technique, such as fitting mutliexponentials to the reference TACs should be performed.

The operation equations (Eqs. (8) and (9)) are first derived to generate parametric images of SRTM. Both computer simulation and human studies show that conventional nonlinear regression with operational Eq. (2) and linear regression with Eq. (8) is comparable for estimating the parameters of SRTM from low noise level of TAC. LRSC is suggested for high noise level of TAC or parametric imaging of SRTM model. Although the BP images generated by WLR with Eq. (9) are of comparable image quality with LRSC, which is consistent with their similar variance, the WLR estimates show more bias than LRSC, especially for pixel TAC of high noise level or ROI TAC of lower receptor density and small volume. It is worth noting that the noise introduced bias (underestimation) was also studied for DV estimation in ligand-receptor PET or single-photon emission computed tomography (SPECT) studies (Slifstein

Table 2
The ROI values on the mean and variance of parametric images generated from 9 human [11C]FMZ and 16 human [11C]RAC dynamic PET studies

| Estimates | [11C]FMZ | | | | | | | | [11C]RAC | |
|---|---|---|---|---|---|---|---|---|---|---|
| | ROIs:<br>Volume (mm$^3$): | Caudate<br>1960 | Cerebellum<br>17520 | Frontal<br>16784 | Occipital<br>9544 | Putamen<br>4008 | Thalamus<br>4496 | | Caudate<br>1960 | Putamen<br>4008 |
| *BP* by LRSC | Mean | 1.38 | 1.99 | 3.48 | 3.89 | 1.55 | 2.00 | | 2.15 | 2.39 |
| | Variance | 0.2334 | 0.5601 | 0.1374 | 0.1708 | 0.1371 | 0.6353 | | 0.5329 | 0.7583 |
| *BP* by LRSC | Mean | 1.50 | 2.07 | 3.58 | 3.98 | 1.65 | 2.12 | | 2.29 | 2.53 |
| (Eq. (8)) | Variance | 0.3026 | 0.7476 | 0.4275 | 0.6747 | 0.2653 | 0.8416 | | 0.7323 | 1.0051 |
| *BP* by WLR | Mean | 1.34 | 1.92 | 3.30 | 3.68 | 1.49 | 1.94 | | 2.05 | 2.28 |
| | Variance | 0.2504 | 0.6517 | 0.1421 | 0.1773 | 0.1404 | 0.7397 | | 0.5694 | 0.8011 |
| *BP* by WLR | Mean | 1.15 | 2.07 | 3.60 | 4.00 | 1.43 | 2.00 | | 2.28 | 2.52 |
| (Eq. (8)) | Variance | 0.5113 | 0.7763 | 1.4743 | 1.8578 | 0.9773 | 0.8744 | | 0.9247 | 1.2205 |
| *BP* by<br>NLRRSC | Mean | 1.42 | 2.00 | 3.39 | 3.83 | 1.70 | 1.96 | | 2.05 | 2.26 |
| | Variance | 0.2643 | 0.6743 | 0.1551 | 0.1910 | 0.1537 | 0.7646 | | 0.5329 | 0.7583 |
| *BP* by<br>WNLRM | Mean | 1.46 | 2.08 | 3.57 | 3.97 | 1.65 | 2.08 | | 2.27 | 2.51 |
| | Variance | 0.3890 | 0.7680 | 0.4195 | 0.4538 | 0.3804 | 0.8412 | | 0.8042 | 1.0768 |
| $R_I$ by LRSC | Mean | 1.27 | 1.19 | 1.14 | 1.19 | 1.36 | 1.46 | | 0.85 | 0.92 |
| | Variance | 0.0276 | 0.0257 | 0.0344 | 0.0486 | 0.0412 | 0.0284 | | 0.0674 | 0.0719 |
| $R_I$ by WLR | Mean | 1.33 | 1.20 | 1.16 | 1.21 | 1.39 | 1.48 | | 0.88 | 0.92 |
| | Variance | 0.0625 | 0.0798 | 0.1061 | 0.1337 | 0.1506 | 0.0813 | | 0.1342 | 0.1269 |
| $R_I$ by<br>NLRRSC | Mean | 1.24 | 1.24 | 1.29 | 1.31 | 1.30 | 1.40 | | 0.78 | 0.83 |
| | Variance | 0.0544 | 0.0791 | 0.0670 | 0.0946 | 0.1018 | 0.0889 | | 0.0950 | 0.0939 |
| $R_I$ by<br>WNLRM | Mean | 1.07 | 1.14 | 1.14 | 1.19 | 1.16 | 1.24 | | 0.80 | 0.85 |
| | Variance | 0.0723 | 0.0826 | 0.1225 | 0.1349 | 0.1616 | 0.0838 | | 0.1200 | 0.1183 |
| $k_2$ by LRSC | Mean | 0.20 | 0.26 | 0.32 | 0.29 | 0.31 | 0.23 | | 0.18 | 0.18 |
| | Variance | 0.0040 | 0.0027 | 0.0057 | 0.0071 | 0.0044 | 0.0034 | | 0.0044 | 0.0045 |
| $k_2$ by WLR | Mean | 0.21 | 0.26 | 0.33 | 0.29 | 0.32 | 0.23 | | 0.19 | 0.19 |
| | Variance | 0.0081 | 0.0054 | 0.0176 | 0.0197 | 0.0181 | 0.0063 | | 0.0064 | 0.0063 |
| $k_2$ by<br>NLRRSC | Mean | 0.31 | 0.28 | 0.33 | 0.29 | 0.31 | 0.32 | | 0.20 | 0.20 |
| | Variance | 0.0078 | 0.0043 | 0.0165 | 0.0136 | 0.0206 | 0.0049 | | 0.0055 | 0.0055 |
| $k_2$ by<br>WNLRM | Mean | 0.39 | 0.30 | 0.34 | 0.30 | 0.32 | 0.39 | | 0.20 | 0.21 |
| | Variance | 0.0145 | 0.0062 | 0.0378 | 0.0379 | 0.0379 | 0.0075 | | 0.0083 | 0.0087 |

and Laruelle, 2000). It was reported that the bias can be introduced by noise of TAC if DV estimated by Logan graphical analysis with plasma input function (Logan et al., 1990), and this underestimation is positively correlated to the high noise level of TAC, which usually occurred at lower receptor density regions. For DV estimated by two-compartmental model (plasma and tissue) with conventional

linear regression, DV was also underestimated if TACs have high noise level (Zhou et al., 2002a).

In fact, Eq. (9) is very similar to the Logan plot with reference TAC as input function (see Eq. (1)). A multilinear method has been derived from the Logan plot (Ichise et al., 1996, 1997) that is fundamentally the same as Eq. (9), since it is also a multilinear equation with three linear components
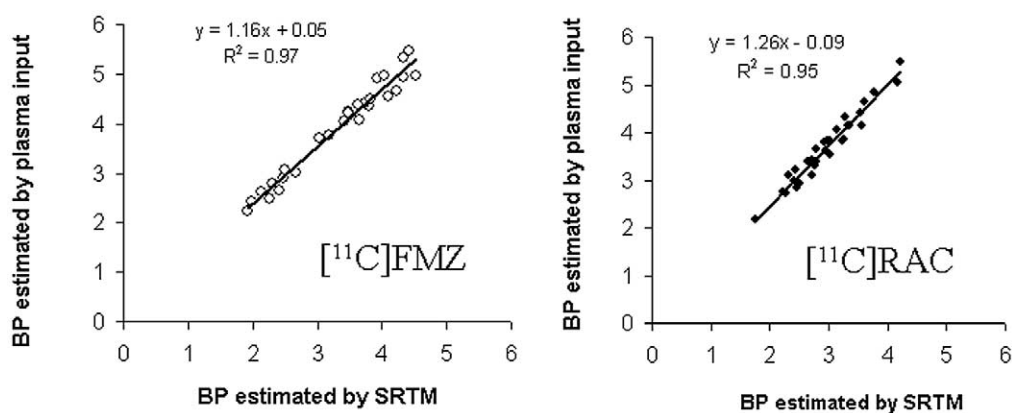


Fig. 8. Based on ROI (see materials and method for ROI determination) kinetic analysis, a strong linear correlation is found between BP estimates obtained using the plasma input model shown in Figs. 1 and SRTM in 9 human [11C]flumazenil ([11C]FMZ) and 16 human [11C]raclopride ([11C]RAC) dynamic PET studies. For plasma input modeling, the value of $K_1/k_2$ was fixed to the distribution volume measured in reference tissue.

with one of the parameters being $DV_R$. In fact, using reference TAC as input, the Logan plot as well as its variations can be considered as a special case of SRTM. This can be easily seen by the following equation resulted from dividing Eq. (9) by $C_T$:

$$\frac{\int_0^t C_T(s)ds}{C_T(t)} = DV_R \frac{\int_0^t C_{REF}(s)ds}{C_T(t)}$$

$$+ DV_R/(k_2/R_1) \frac{C_{REF}(t)}{C_T(t)} - (DV_R/k_2).$$

Note that $k_{2R} = k_2/R_1$. Thus, for tissue time activity curves of low noise level, the Logan plot and the Eq. (9) derived from SRTM are fundamentally the same equation for BP estimation. Statistically, the BP estimated using Eq. (9) or the above equation derived from Logan plot can be considered as a special technique to minimize the variance of estimates by estimating ratio without division, if it is compared to the BP estimated using Eq. (8) (Lange, 1999). Based on conventional ROI kinetic analysis, the Logan plot and SRTM with Eq. (2) provides almost identical estimates of BP (Sossi et al., 2001). It is expected that the BP is also underestimated by Logan plot or its variation (Ichise et al., 1996, 1997), and this underestimation is also due to noise of TAC and model approximation.

In this study, the parameters estimated by conventional nonlinear regression using operational Eq. (2) were compared to those estimated by linear regression and LRSC using computer simulation, a lower noise level of ROI TACs, and a high noise level of pixel TAC. At the lower noise level of simulated data or ROI TACs, all methods give almost same estimates. Nonlinear regression is very sensitive to the noise level of tissue TAC, which can result in intrinsic nonlinear problems such as local minimums and convergence, nonlinear estimators can also become biased estimators at a high noise level of TACs. In this study we have demonstrated that the linear estimator is more accurate than a nonlinear estimator although there is a small bias contributed from integration into the linear estimator. We also found that the accuracy of conventional WLR estimates of $R_1$ and $k_2$ is markedly improved by general ridge regression with spatial constraint. It is necessary to clarify, however, that greater accuracy of parameter estimates does not necessarily correspond to the best fit of measured TAC. In fact a better fit, as judged by a lower residual sum square in kinetic space, is usually at the cost of higher spatial variation in parameter space (Zhou et al., 2002c).

When applying the linear GRRSC algorithm used in LRSC, a high-pass filter is recommended to be used in the filtered backprojection reconstruction to maintain high spatial resolution in the dynamic images. This ensures optimal trade-off between noise depression and spatial resolution loss that can be produced by GRRSC when generating

parametric images. In addition, the spatial smoothing filter (equal weighting over all pixels within given window in plane) selected for LRSC in the current study originated from the criterion of minimizing local variation in the parametric image. In fact, any filter could be used in the LRSC, and its selection is always dependent on the noise level of the dynamic images. Note that LRSC is not sensitive to the smoothing filter, and this is consistent with results obtained in our previous studies (Zhou et al., 2001, 2002a, 2002b, 2002c). Although the smoothing filter for spatial constraint is the same for the parametric image generation algorithms using Eqs. (8) and (9) of LRSC, they have different effects on the parametric images. For $R_1$ and $k_2$, the spatial constraint is automatically adjusted by both the variance of pixel kinetics and the variance of estimates, based on the GRRSC theory. Therefore, the resolution loss of $R_1$ and $k_2$ images due to spatial constraint is not spatially uniform, and the $k_2$ images have lower spatial resolution. For the BP, the selection of the applied smoothing filter is somewhat arbitrary. However, based on the theory (see subsection "Parametric image generation algorithm using Eq. (9)"), and the results (WLR versus LRSC) of computer simulations and human studies, the BP estimates obtained with LRSC are quite robust to the spatial constraint in terms of the variance and resolution loss. In fact, the results from human studies demonstrate that the resolution of BP images generated by LRSC and WLR is visually comparable. Additionally, BP obtained using Eq. (9) is not sensitive to the weighting for linear regression, since the output measurements $\int_0^t C_T(s)ds$ is of low noise level (see Materials and methods). Note that the regression weighting for model fitting is chosen to be proportional to the scan length in the present study. Strictly speaking, $W_{ii}$, as chosen in our computer simulation, should be related to the scan length of the frame and is inversely related to the average counts in the frame for parameter estimation using Eq. (2) or Eq. (8) (Chen et al., 1991). In practice, however, we find that the use of the scan length to approximate $W_{ii}$ gives good and robust results for generating parametric images (Zhou et al., 2001, 2002a, 2002b, 2002c).

In summary, in contrast to nonlinear regression using Eq. (2), utilization of the operational Eqs. (8) and (9) of integral form derived from a simplified reference tissue model are simpler, more robust, and more computationally efficient for parameter estimation. For LRSC, results from computer simulations and human studies show that the variance of estimates is reduced by ridge regression while the bias of estimates is limited by the spatial constraint. This finding is consistent with ridge regression theory (Hoerl and Kennard, 1970a, 1970b), and the results obtained in the previous studies (Zhou et al., 2001, 2002c). We conclude that the new linear equations yield a reliable, computationally efficient, and robust LRSC algorithm that is suggested to generate parametric images of ligand-receptor dynamic PET studies with SRTM.

## Acknowledgments

## References

Banati, R.B., Goerres, G.W., Myers, R., Gunn, R.N., Turkheimer, F.E., Kreutzberg, G.W., Brooks, D.J., Jones, T., Duncan, J.S., 1999. [$^{11}$C](R)-PK11195 positron emission tomography imaging of activated microglia in vivo in Rasmussen's encephalitis. Neurology 53, 2199–2203.

Blomqvist, G., 1984. On the construction of functional maps in positron emission tomography. J. Cereb. Blood Flow Metab. 4, 629–623.

Blomqvist, G., Pauli, S., Farde, L., Eriksson, L., Persson, A., Halldin, C., 1990. Maps of receptor binding parameters in the human brain—a kinetic analysis of PET measurements. Eur. J. Nucl. Med. 16, 257–265.

Blomqvist, G., Tavitian, B., Pappata, S., Crouzel, D., Jobert, A., Doignon, I., Di Giamberardino, L., 2001. A tracer kinetic model for measurement of regional acetylcholinesterase activity in the brain using [$^{11}$C]physostigmine and PET, in: Gjedde, A., Hansen, S.B., Knudsen, G.M., Paulson, O.B. (Eds.), Physiological Imaging of the Brain with PET, Academic Press, San Diego, pp. 273–278.

Carson, R.E., Channing, M.A., Blasberg, R.G., Dunn, B.B., Cohen, R.M., Rice, K.C., Herscovitch, P., 1993. Comparison of bolus and infusion methods for receptor quantitation: application to [$^{18}$F]cyclofoxy and positron emission tomography. J. Cereb. Blood Flow Metab. 13, 24–42.

Carson, R.E., Huang, S.-C., Green, M.V., 1986. Weighted integration method for local cerebral blood flow measurements with positron emission tomography. J. Cereb. Blood Flow Metab. 16, 245–258.

Chen, K., Huang, S.C., Yu, D.C., 1991. The effects of measurement errors in the plasma radioactivity curve on parameter estimation in positron emission tomography. Phys. Med. Biol. 36, 1183–1200.

Chen, K., Lawson, M., Reiman, E., Cooper, A., Feng, D., Huang, S.C., Bandy, D., Ho, D., Yun, L.S., Palant, A., 1998. Generalized linear least squares method for fast generation of myocardial blood flow parametric images with N-13 ammonia PET. IEEE Trans. Med. Imag. 17, 236–243.

Cherry, S.R., Meikle, S.R., Hoffman, E.J., 1993. Correction and characterization of scattered events in three-dimensional PET using scanners with retractable septa. J. Nucl. Med. 34, 671–678.

Delforge, J., Spelle, L., Bendriem, S.B., Samson, Y., Syrota, A., 1997. Parametric images of benzodiazepine receptor concentration using a partial-saturation injection. J. Cereb. Blood Flow Metab. 17, 343–355.

Endres, C.J., Carson, R.E., 1998. Assessment of dynamic neurotransmitter changes with bolus or infusion delivery of neuroreceptor ligands. J. Cereb. Blood Flow Metab. 18, 1196–1210.

Evans, A.C., Marrett, S., Torrescorzo, J., Ku, S., Collins, L., 1991. MRI-PET correlation in three dimensions using a volume-of-interest (VOI) atlas. J. Cereb. Blood Flow Metab. 11, A69–A78.

Farde, L., Eriksson, L., Blomquist, G., Halldin, C., 1989. Kinetic analysis of central [$^{11}$C]raclopride binding to D2-dopamine receptors studied by PET—a comparison to the equilibrium analysis. J. Cereb. Blood Flow Metab. 9, 696–708.

Feng, D., Wong, Z., Huang, S.C., 1993. A study on statistically reliable and computationally efficient algorithms for generating local cerebral blood flow parametric images with positron emission tomography. IEEE Trans. Med. Imag. 12, 182–188.

Frost, J.J., Douglass, K.H., Mayberg, H.S., Dannals, R.F., Links, J.M., Wilson, A.A., Ravert, H.T., Crozier, W.C., Wagner Jr., H.N., 1989. Multicompartmental analysis of [$^{11}$C]-carfentanil binding to opiate receptors in humans measured by positron emission tomography. J. Cereb. Blood Flow Metab. 9, 398–409.

Ginovart, N., Wilson, A.A., Meyer, J.H., Hussey, D., Houle, S., 2001. Positron emission tomography quantification of [11C]-DASB binding to the human sertonin transporter: modeling strategies. J. Cereb. Blood Flow Metab. 21, 1342–1353.

Gunn, R.N., Gunn, S.R., Cunningham, V.J., 2001. Positron emission tomography compartmental models. J. Cereb. Blood Flow Metab. 21, 635–652.

Gunn, R.N., Lammertsma, A.A., Hume, S.P., Cunningham, V.J., 1997. Parametric imaging of ligand-receptor binding in PET using a simplified reference region model. NeuroImage 6, 279–287.

Gunn, R.N., Sargent, P.A., Bench, C.J., Rabiner, E.A., Osman, S., Pike, V.W., Hume, S.P., Grasby, P.M., Lammertsma, A.A., 1998. Tracer kinetic modeling of the 5-HT$_{1A}$ receptor ligand [carbonyl-$^{11}$C]WAY-100635 for PET. NeuroImage 8, 426–440.

Herholz, K., 1987. Nonstational spatial filtering and accelerated curve fitting for parametric imaging with dynamic PET. Eur. J. Nucl. Med. 14, 477–484.

Hoerl, A.E., Kennard, R.W., 1970a. Ridge regression: applications to nonorthogonal problems. Technometrics 12, 69–82.

Hoerl, A.E., Kennard, R.W., 1970b. Ridge regression: biased estimation for nonorthogonal problems. Technometrics 12, 55–67.

Holden, J.E., Sossi, V., Chan, G., Doudet, D.J., Stoessl, A.J., Ruth, T.J., 2001. Effect of population $k_2$ values in graphical estimation of DV ratios of reversible ligands, in: Gjedde, A., Hansen, S.B., Knudsen, G.M., Paulson, O.B. (Eds.), Physiological Imaging of the Brain with PET, Academic Press, San Diego, pp. 127–129.

Huang, S.-C., Zhou, Y., 1998. Spatially-coordinated regression for image-wise model fitting to dynamic PET data for generating parametric images. IEEE Trans. Nucl. Sci. 45, 1194–1199.

Ichise, M., Ballinger, J.R., Golan, H., et al., 1996. Noninvasive quantification of dopamine D2-receptors with iodine-123-IBF SPECT. J. Nucl. Med. 37, 513–520.

Ichise, M., Ballinger, J.R., Vines, D., Tsai, S., Kung, H.F., 1997. Simplified quantification and reproducibility studies of dopamine D2-receptor binding with Iodine-123-IBF SPECT in health subjects. J. Nucl. Med. 38, 31–37.

Kimura, Y., Senda, M., Alpert, N.M., 2002. Fast formation of statistically reliable FDG parametric images based on clustering and principal components. Phys. Med. Biol. 47, 455–68.

Koeppe, R.A., Holthoff, V.A., Frey, K.A., Kilbourn, M.R., Kuhl, D.E., 1991. Compartmental analysis of [$^{11}$C]flumazenil kinetics for the estimation of ligand transport rate and receptor distribution using positron emission tomography. J. Cereb. Blood Flow Metab. 11, 735–744.

Koeppe, R.A., Frey, K.A., Vander Borght, T.M., Karlamangla, A., Jewett, D.M., Lee, L.C., Kilbourn, M.R., Kuhl, D.E., 1996. Kinetic evaluation of [$^{11}$C]dihydrotetrabenazine by dynamic PET: measurement of vesicular monoamine transporter. J. Cereb. Blood Flow Metab. 16, 1288–1299.

Lammertsma, A.A., Bench, C.J., Hume, S.P., Osman, S., Gunn, K., Brooks, D.J., Frackowiak, R.S.J., 1996. Comparison of methods for analysis of clinical [$^{11}$C]raclopride studies. J. Cereb. Blood Flow Metab. 16, 42–52.

Lammertsma, A.A., Hume, S.P., 1996. Simplified reference tissue model for PET receptor studies. NeuroImage 4, 153–158.

Lange, K., 1999. Numerical Analysis for Statisticians. Springer-Verlag, New York.

Lassen, N.A., Bartenstein, P.A., Lammertsma, A.A., Prevett, M.C., Turton, D.R., Luthra, S.K., Osman, S., Bloomfield, P.M., Jones, T., Patsalos, P.N., O'Connell, M.T., Duncan, J.S., Vanggaard Andersen, J., 1995. Benzodiazepine receptor quantification in vivo in humans using [$^{11}$C]flumazenil and PET: application of the steady-state principal. J. Cereb. Blood Flow Metab. 15, 152–165.

Lawton, W.H., Sylvestre, E.A., 1971. Elimination of linear parameters in nonlinear regression. Technonmetrics 13, 461–467.

Logan, J., Fowler, J.S., Volkow, N.D., et al., 1990. Graphical analysis of reversible radioligand binding from time-activity measurements applied to [N-11C-methuyl]-(−)-cocaine PET studies in human subjects. J. Cereb. Blood Flow Metab. 10, 740–747.

Logan, J., Fowler, J.S., Volkow, N.D., Wang, G-J., Ding, Y-S., Alexoff, D.L., 1996. Distribution volume ratios without blood sampling from graphic analysis of PET data. J. Cereb. Blood Flow Metab. 16, 834–840.

Lopresti, B.J., Mathis, C.A., Price, J.C., Villemagne, V., Meltzer, C.C., Holt, D.P., Smith, G.S., Moore, R.Y., 2001. Serotonin transporter binding in vivo: further examination of [11C]McN5652, in: Gjedde, A., Hansen, S.B., Knudsen, G.M., Paulson, O.B. (Eds.), Physiological Imaging of the Brain with PET, Academic Press, San Diego, pp. 265–271.

Marquardt, D.W., 1963. An algorithm for least-squares estimations of nonlinear parameters. J. Soc. Ind. Appl. Math. 11, 431–441.

Millet, P., Graf, C., Buck, A., Walder, B., Ibanez, V., 2002. Evaluation of the reference tissue models for PET and SPECT benzodiazepine binding parameters. NeuroImage 17, 928–942.

Mintun, M.A., Raichle, M.E., Kilbourn, M.R., Wooten, G.F., Welch, M.J., 1984. A quantitative model for the in vivo assessment of drug binding sites with positron emission tomography. Ann Neurol. 15, 217–227.

O'Sullivan, F., 1994. Metabolic images from dynamic positron emission tomography studies. Stat. Methods Med. Res. 3, 87–101.

Parsey, R.V., Slifstein, M., Hwang, D.-R., Abi-Dargham, A., Simpson, N., Guo, N., Shinn, A., Mawlawi, O., Van Heertum, R., Mann, J.J., Laruelle, M., 2001. Comparison of kinetic modeling methods for the in vivo quantification of 5-HT$_{1A}$ receptors using WAY 100635, in: Gjedde, A., Hansen, S.B., Knudsen, G.M., Paulson, O.B. (Eds.), Physiological Imaging of the Brain with PET, Academic Press, San Diego, pp. 249–255.

Patlak, C.S., Blasberg, R.G., 1985. Graphical evaluation of blood-to-brain transfer constants from multiple-time uptake data: generalizations. J. Cereb. Blood Flow Metab. 5, 584–590.

Price, J.C., Mayberg, H.S., Dannals, R.F., Wilson, A.A., Ravert, H.T., Sadzot, B., Rattner, Z., Kimball, A., Feldman, M.A., Frost, J.J., 1993. Measurement of benzodiazepine receptor number and affinity in humans using tracer kinetic modeling, positron emission tomography, and [$^{11}$C]flumazenil. J. Cereb. Blood Flow Metab. 13, 656–667.

Slifstein, M., Laruelle, M., 2000. Effects of statistical noise on graphic analysis of PET neuroreceptor studies. J. Nucl. Med. 41, 2083–2088.

Sossi, V., Holden, J.E., Chan, G., Krzywinski, M., Stoessl, A.J., Ruth, T.J., 2001. Measuring the BP of four dopaminergic tracers utilizing a tissue input function, in: Gjedde, A., Hansen, S.B., Knudsen, G.M., Paulson, O.B. (Eds.), Physiological Imaging of the Brain with PET, Academic Press, San Diego, pp.131–137.

Szabo, Z., Scheffel, U., Mathews, W.B., Ravert, H.T., Szabo, K., Kraut, M., Palmon, S., Ricaurte, G.A., Dannals, R.F., 1999. Kinetic analysis of [$^{11}$C]McN5652: a serotonin transporter radioligand. J. Cereb. Blood Flow Metab. 19, 967–981.

Wagner Jr., H.N., Burns, H.D., Dannals, R.F., Wong, D.F., Langstrom, B., Duelfer, T., Frost, J.J., Ravert, H.T., Links, J.M., Rosenbloom, S.B., Lukas, S.E., Kramer, A.V., Kuhar, M.J., 1983. Imaging dopamine receptors in the human brain by positron emission tomography. Science 221, 1264–1266.

Wong, D.F., Wagner Jr., H.N., Dannals, R.F., et al., 1984. Effects of age on dopamine and serotonin receptors measured by positron tomography in the living human brain. Science 226, 1393–1396.

Wong, D.F., Yung, B., Dannals, R.F., Shaya, E.K., Ravert, H.T., Chen, C.A., Chan, B., Folio, T., Scheffel, U., Ricaurte, G.A., Neumeyer, J.L., Wagner Jr., H.N., Kuhar, M.J., 1993. In vivo imaging of baboon and human dopamine transporters by positron emission tomography using [$^{11}$C]WIN35,428. Synapse 15, 130–142.

Zhou, Y., Huang, S.C., Bergsneider, M., 2001. Linear ridge regression with spatial constraint for generation of parametric images in dynamic positron emission tomography studies. IEEE Trans. Nucl. Sci. 48, 125–130.

Zhou, Y., Brasic, J.R., Musachio, J.L., et al., 2002a. Human [$^{123}$I]5-I-A-85380 dynamic SPECT studies in normals: kinetic analysis and parametric imaging. Proc. IEEE Nucl. Sci. Symp. Med. Imag. 1335–1340.

Zhou, Y., Huang, S.C., Bao, S., Wong, D.F., 2002b. Parametric imaging and statistical mapping of brain tumor in Ga-68 EDTA dynamic PET studies. Proc. IEEE Nucl. Sci. Symp. Med. Imag. 1072–1078.

Zhou, Y., Huang, S.C., Bergsneider, M., Wong, D.F., 2002c. Improved parametric image generation using spatial-temporal analysis of dynamic PET studies. NeuroImage 15, 697–707.